On the influence of virtual camber effect on airfoil polars for use in simulations of Darrieus wind turbines

Publisher's version at DOI: 10.1016/j.enconman.2015.09.053

On the Influence of Virtual Camber Effect on Airfoil Polars for Use in Simulations of Darrieus Wind Turbines

Alessandro Bianchini[1a], Francesco Balduzzi[1b], John M. Rainbird[2c*], Joaquim Peiro[2d], J. Michael R. Graham[2e], Giovanni Ferrara[1f], Lorenzo Ferrari[3g]

[1)] Department of Industrial Engineering, University of Florence
Via di Santa Marta 3, 50139, Florence, Italy
Phone +39 055 275 8773

[2)] Department of Aeronautical Engineering, Imperial College
South Kensington Campus, SW7 2AZ, London, UK
* Phone +44 (0)20 7594 5074

[3)] CNR-ICCOM, National Research Council of Italy
Via Madonna del Piano 10, 50019, Sesto Fiorentino, Italy
Phone +39 055 5225 218 - Fax +39 055 5225 203

Abstract

Darrieus vertical-axis wind turbines are experiencing renewed interest from researchers and manufacturers, though their efficiencies still lag those of horizontal-axis wind turbines. A better understanding of their aerodynamics is required to improve on designs, for example through the development of more accurate low-order (e.g. blade element momentum) models. Many of these models neglect the impact of the curved paths that are followed by blades on their performance. It has been theorized that the curved streamlines of the flow impart a virtual camber and incidence on them, giving a performance analogous to a cambered blade in a rectilinear flow.

To test the extent of this effect, wind tunnel experiments have been conducted in a rectilinear flow to obtain lift and drag for three airfoils: a NACA 0018 and two conformal transforms of the profile. The transformed airfoils exhibit the virtual camber that the theory predicts is imparted to a NACA 0018 when used in a Darrieus turbine with blade chord-to-turbine radius ratios, *c/R*, of 0.114 and 0.25. A parallel computational fluid dynamics campaign has been conducted to study the

a) bianchini@vega.de.unifi.it *b) balduzzi@vega.de.unifi.it*
c) j.rainbird11@imperial.ac.uk *d) j.peiro@imperial.ac.uk*
e) m.graham@imperial.ac.uk *f) giovanni.ferrara@unifi.it*
g) lorenzo.ferrari@iccom.cnr.it (=corresponding author)*

aerodynamic behavior of the same blades in curvilinear flow in Darrieus-like motion with *c/R* = 0.114 and 0.25, at tip-speed ratios of 2.1 and 3.1, using novel techniques to obtain blade effective angles of attack. The analysis confirms that the theory holds, with the wind tunnel results for the NACA 0018 being analogous to numerical results for the relevant cambered airfoils.

In addition, turbine performance is calculated using computational fluid dynamics and a blade element momentum code, for each of the blades in turn. The computational fluid dynamics results for the NACA 0018 agree closely to blade element momentum results for the equivalent cambered airfoil where *c/R* = 0.25, for both turbine power and blade tangential forces. Agreement between the two methods using geometrically identical blades is poor at both the blade and turbine level for *c/R* = 0.25.

It is concluded that when modeling a Darrieus rotor using blade element momentum methods, applying experimental data for the profile used in the turbine will yield inaccurate results if the *c/R* ratio is high, in such cases it is necessary to select a profile based on the virtual shape of the blades.

Keywords: Darrieus, vertical axis wind turbine, flow curvature, virtual camber, experiments, CFD, blockage tolerant wind tunnel

1. Introduction

Most installed wind energy capacity is provided by large wind farms comprised of horizontal axis wind turbines (HAWTs) [1]. Turbines are becoming ever more efficient and their diameters ever bigger. While these large installations are a valuable addition to grid capacity, such designs are not suitable for building integration, and they do not benefit people and communities without a grid connection.

Installed capacity comprised of smaller turbines, both on- and off-grid, is growing in the U.S. [2] with similar trends notable in other developed countries. Research into novel small designs is also on the increase. Building integration forms a large part of this, with studies looking at the

challenges presented by the pre-existing built environment [3,4] or aiming to design new buildings that produce favorable conditions for wind energy production [5].

Vertical axis wind turbines (VAWTs) have been identified as suitable for small-scale installations due to their mechanical simplicity and ease of installation and maintenance afforded by the positioning of generation equipment at ground level [6]. Recent studies have focused on the integration of VAWTs into the built environment, e.g. in rooftop installations [7] or in skewed flows caused by urban infrastructure [8,9], and on improvement of VAWT energy yields [10], which still lag conventional HAWTs.

VAWTs are also suited to urban installations due to their good handling of turbulent and unstructured flows, with low noise emissions and high reliability [11]. Darrieus rotors are the most popular VAWT design used, as they are the only VAWT able to reach power coefficients comparable to HAWTs [12].

To improve efficiencies further, a more in depth understanding of the physical phenomena that govern Darrieus turbine behavior is needed. For example, both dynamic stall [12] and flow curvature effects [13] affect turbine performance, but are not completely understood. Approximate corrections, or no correction at all, are applied for them when using low-order models (e.g. blade-element momentum, BEM models). Low-order models still represent an industry standard for the analysis of wind turbines. Whether used as a first step in the design process, or in coupled codes for the analysis of aero and other dynamics simultaneously [14], they are used ahead of more advanced analyses due to their robustness and speed. Reasonably accurate results have been produced for time-dependent studies on acceleration [15] and for power and operating range calculations [16].

Studies have demonstrated that so-called “flow curvature effects” have a large impact on small Darrieus turbine performance. These effects, caused by the curved paths that VAWT blades follow in operation, were first proposed by Migliore [17]. They manifest in a “virtual” blade camber and incidence, giving blade performance characteristics analogous to those of a cambered blade at incidence in a rectilinear flow. Migliore never went beyond his theoretical approach to verify his

proposals experimentally. The current authors have conducted several numerical and experimental studies in an attempt to verify Migliore's theory.

Initial research compared BEM output, using polars for symmetrical airfoils and cambered airfoils, to experimental turbine data [18]. The cambered airfoil data was taken from literature and gives only an approximate representation of virtual camber effects. Later, a technique was developed to find the effective incidence of VAWT blades in computational fluid dynamics (CFD) simulations [13]. This allowed plots of airfoil lift and drag against incidence to be processed from the turbine CFD data. CFD results for a turbine with virtually cambered blades were compared to experimental results for a symmetrical NACA 0018 from literature.

This paper documents a new approach to the problem. Rather than relying on existing blade polars for symmetrical airfoils, or cambered profiles that represent, at best, an approximation to virtual camber, new wind tunnel experiments have been conducted. Lift and drag forces have been obtained for three airfoils: a NACA 0018 and two modified profiles based on the NACA 0018. The modified profiles have been conformally transformed to fit their camber lines to the arc of a circle, such that the ratio of the airfoil chord to the circle's radius, *c/R*, is 0.114 or 0.25. See Fig. 3 for the three profiles. Wind tunnel testing has used a new, blockage tolerant test section specifically developed for VAWT blade testing [19].

The NACA 0018 was chosen as it is commonly used in VAWT research, while the *c/R* ratios of the transformed airfoils were chosen for comparability to those used in Migliore's original paper of 0.114 and 0.26 [17]. The airfoil with *c/R* of 0.114 has a maximum camber of 1.42% at 50% of chord, while the *c/R* of 0.25 has 3.11% maximum camber, again at 50% of chord.

Based on Migliore's proposal, in the flow of the wind tunnel the transformed airfoils should perform as the unmodified NACA 0018 would in VAWTs with similar *c/R* ratios and conversely the NACA 0018's tunnel results should be similar to those of the transformed airfoils when used in the VAWTs. Obtaining force data from a rotating VAWT blade would be challenging experimentally. Instead, CFD simulations have been conducted at several tip-speed ratios, TSRs.

Results for TSRs of 2.1 and 3.1 are presented in this paper. Forces calculated have been processed into plots of lift and drag against effective incidence using the aforementioned technique [13].

Preliminary findings, comparing data obtained in a conventional wind tunnel (for just the NACA 0018 and the *c/R* of 0.25 transform) to CFD results (for turbines with *c/R* of 0.25), have been published previously [20] with limited consideration of BEM modeling. This paper extends the work to two transformed airfoil and turbine *c/R* ratios, using new wind tunnel results from the blockage tolerant test section and higher quality CFD results. It also provides an analysis of what these findings mean for BEM modeling of VAWTs, including recommendations of how best to account for the virtual camber effect in such codes.

The experiments and simulations documented in this paper were conducted at a Reynolds number of 300,000. This is a typical operating blade Reynolds number for small-scale, commercially available VAWTs. For example, the Urban Green Energy Visionair 3 turbine [21], has a 1.8 m diameter and 0.38 m blade chord. In normal operating conditions, at a TSR of 3 in a wind speed of 6 m/s, it will experience blade Reynolds numbers of 300,000 – 600,000.

In the range of Reynolds numbers a VAWT blade could be expected to encounter (less than 3×10^6 for even the largest VAWTs in high winds), other than at very low Reynolds numbers (of less than 80,000), the addition of camber to a profile has the same effects on airfoil performance. These can be seen in Fig. 8, namely a shift in the lift/incidence curve to higher lifts, an increase in positive stall angle (and the maximum lift generated at this point) and a corresponding decrease in negative stall angle (and the minimum lift generated at this point). See for example the low Reynolds number work of Selig [22] and Althaus [23]. This has been confirmed in the range 80,000 – 300,000 for the profiles used in this study in wind tunnel tests conducted by the current authors that are yet to be published. Thus, testing the validity of Migliore's theory at one Reynolds number in this range gives confidence in its applicability to all relevant Reynolds numbers.

The *c/R* ratio used here, after Migliore [17], is a measure of virtual camber added to a blade undergoing VAWT motion. It is subtly different to the more common turbine solidity ratio, *Nc/R*,

where N is the number of blades on the rotor, since it is independent of blade number. This paper shows that while virtual camber does not greatly impact turbines with a c/R of 0.114, it does those with a c/R of 0.25, proving similar for higher c/R turbines. As a point of reference, the Visionair 3 turbine has a c/R of around 0.4, the highest of the Urban Green Energy range.

2. Methods: experiments

Conventional wind tunnels do not provide an accurate reproduction of unconstrained steady flow, since they are conducted using test sections with solid walls which affect the flow around a model under test. The walls constrain any streamline curvature induced by the model. Further, model and walls together block the flow through the tunnel, causing it to speed up. Fig. 1 shows streamline development around an airfoil in a wind tunnel and in free air. The figure was prepared using a panel method with airfoil panels represented by distributed vortices and sources and tunnel wall panels represented by point vortices. The streamlines in both cases are released from the same points. Those constrained by the tunnel show less curvature than the free air equivalents, and are forced closer together by the blockage of the airfoil and tunnel walls.

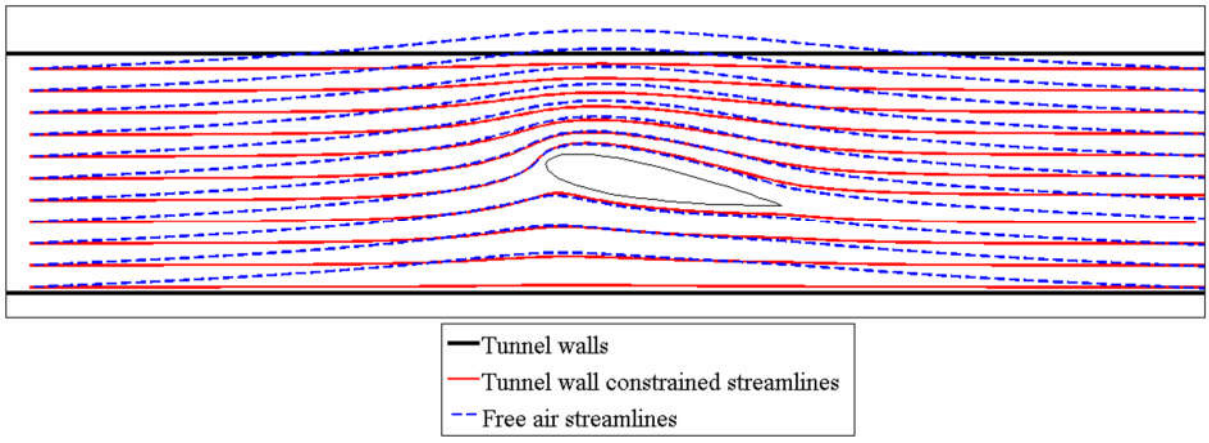

Figure 1 – Effects of wind tunnel walls on streamlines around an airfoil.

2.1 Blockage reduction

151 Blockage corrections are used to compensate for the effect of blockage and streamline
152 curvature. Derived using potential flow theory for streamline constraints and through potential flow
153 and empirical methods for blockage, they are applicable only to attached flows, though with caution
154 they can be applied to flows with "some degree of separation… with caution" [24].
155 Though most testing for this study has been conducted at incidences between the stall angles of
156 the airfoils where corrections perform well, it has extended beyond stall. Tunnel constraints can
157 affect stall itself, with the blockage-accelerated flow resulting in a shift of the stall angle [25].
158 Blockage corrections cannot account for this. Even small differences in airfoil polars have a large
159 impact on VAWT analyses prepared using them [26], so better ways of limiting the effects of
160 blockage are needed for VAWT blade testing. Blockage tolerant wind tunnels offer an alternative
161 means of reducing blockage that is not reliant on corrections. Since corrections for solid-walled and
162 open jet wind tunnels are of opposite signs [24] one would expect that free-air conditions could be
163 approximated using semi-permeable walls.

164 **2.2 The Imperial College Parkinson blockage tolerant tunnel**

165 Parkinson's tunnel design [27] has been used in this study, whose configuration is depicted in
166 Fig. 2. Slotted walls comprised of a regular array of evenly spaced airfoils perpendicular to the flow
167 allow flow to exit and re-enter the main channel, the shape of the array components avoiding
168 separation around them. The slatted wall regions are enclosed by plenum chambers of depth p and
169 length L to maintain mass conservation in the flow along the tunnel. An appropriate open area ratio
170 (OAR, a measure of open to slatted wall areas, defined as g/s) must be settled on through
171 experiments on models of different sizes but with like shapes. The OAR that gives the most similar
172 results for the models is that which provides the closest approximation of unconstrained steady
173 flow, since in free-air results would be identical.
174

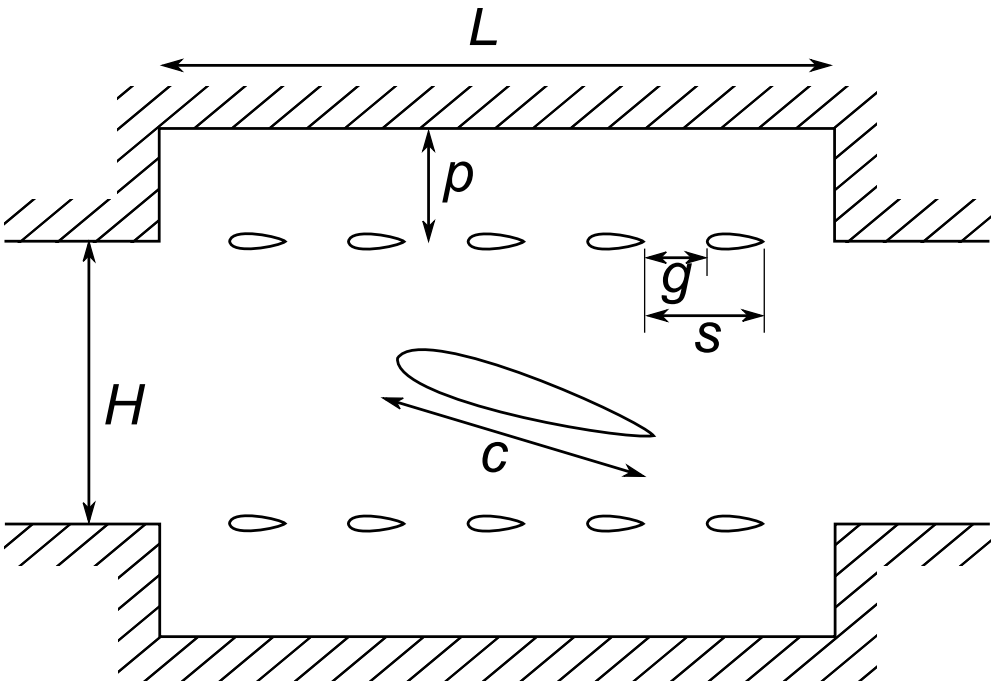

Figure 2 – Schematic diagram of the Parkinson blockage-tolerant wind tunnel.

An OAR of 71% was found to work best for airfoils tested in the Imperial College Parkinson tunnel. The tunnel has a square cross-section with sides of 915mm, a plenum length of 2178mm and depth of 350mm. Slat airfoils have NACA 0015 profiles and 90mm chords.

For details on the design and build of this tunnel, experimental set up, and the experiments performed to calibrate the OAR, see [19]. For convenience, a summary of the experimental set up and methods is given below. The tunnel was found to reduce the effects of blockage better than corrections applied to results taken in a solid-walled tunnel [19]. Data from the tunnel requires no additional processing to achieve low blockage results.

2.3 Airfoils

The three airfoils (the NACA 0018 and transformed airfoils c/R = 0.114 and 0.25, see Fig. 3 for the profiles used) all span the width of the tunnel of 915mm and have 183mm chords to give a chord-to-tunnel height ratio, c/H, of 0.2. They were 3D-printed using nylon laser sintering, in four span-wise parts due to print chamber limitations.

The printed parts were assembled around two 10mm thick 915mm steel rods and were finished with filler and paints to achieve an accurate profile, checking against laser-cut female profile templates produced to an accuracy of < 100 μm. All of the airfoils had their trailing edges blunted to a radius of 0.75 mm to ease the 3D printing process. Note that chord measurements are to this blunted trailing edge.

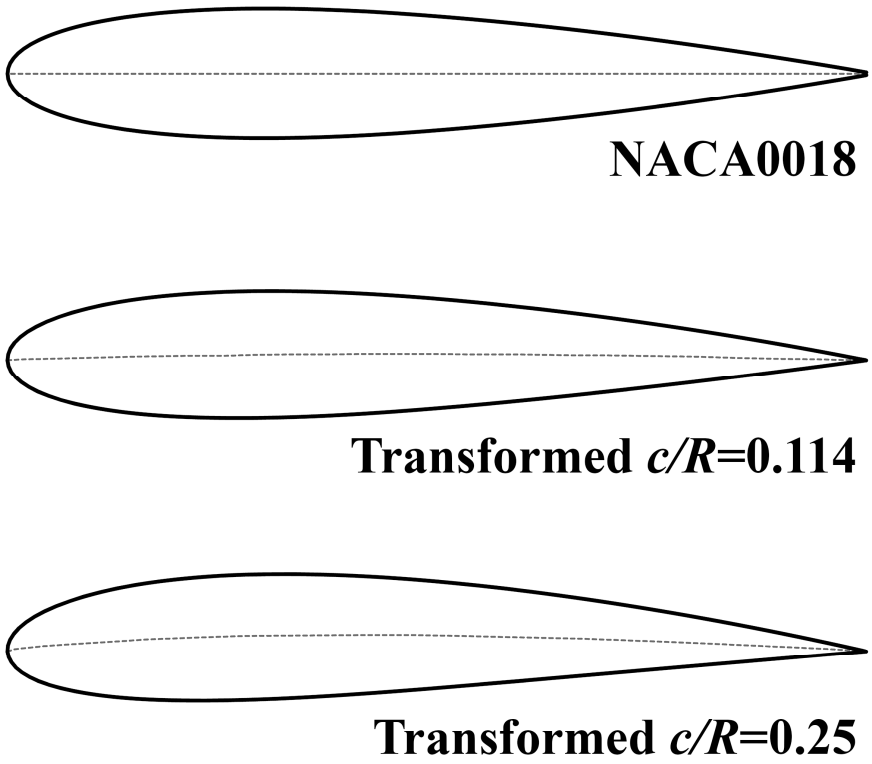

Figure 3 - The three airfoils used in this study.

2.4 Airfoil mounting and force measurement

Airfoils are mounted vertically at the half-chord, between two end plates that sit flush with the tunnel walls. The wind tunnel boundary layer was found to have a negligible impact on results, making this arrangement acceptable.

Force transducers are mounted at both ends of the airfoil, one connected to a bearing, the other to a bearing and a stepper motor to control incidence. The transducers rotate with the airfoil and measure normal and tangential forces along with moment about the half chord.

206 **2.5 Data acquisition and experiment control**

207 Tunnel velocity is measured across the contraction with a manometer and controlled, via outputs
208 on a National Instruments USB-6229 data acquisition board, using a PC running a proportional-
209 integral-derivative controller (PID). The incidence stepper motor is also controlled through the
210 board, with incidence checks taken using an optical encoder to ensure the stepper motor does not
211 slip under load. Outputs from the force transducers are digitized using a pair of NI PCI-6220 data
212 acquisition boards, with simultaneous acquisition from both. These are then processed into lift, drag
213 and moment about the quarter-chord.

214 The process is fully automated and run from a Matlab script. Required incidences and Reynolds
215 number are input, the apparatus does the rest, rotating to each incidence in turn, checking the speed
216 of the tunnel with the PID, allowing settling time, then recording forces and flow conditions.

217 **2.6 Accuracy of measurements**

218 The force transducers used are factory rated to a 95% confidence level to within 1% for force
219 measurements and 1.5% for torque measurements, with no significant deterioration in performance
220 noted.

221 A small amount of play remains in the system when the stepper motor is holding a steady
222 incidence. This is around ±0.25° when forced by hand, though no significant incidence play was
223 noted during experiments over the range of incidences presented in this paper.

224 The largest source of error results from creep in the force transducers. The number of readings
225 taken between re-zeroing of the transducers has been limited to reduce the impact of this. Offsets
226 are taken at the beginning and end of each run of the experiment, with the differences between the
227 two offsets time apportioned across readings to give a local zero from which forces are calculated.
228 The maximum cumulative error in lift or drag readings is estimated at 3%. No differences were
229 noted between repeated runs of the experiments greater than this.

3. Methods: CFD simulations

CFD simulations were used to investigate the aerodynamic behavior of the selected airfoils when rotating in a Darrieus turbine. Four single-bladed rotors were considered, the two *c/R* ratios of 0.114 and 0.25, fitted with both the NACA 0018 and the relevant transformed airfoil.

3.1 Numerical settings and test plan

The commercial code ANSYS Fluent [28] was used to solve the time-dependent unsteady Reynolds-averaged Navier-Stokes (U-RANS) equations in their two-dimensional form. Based on previous studies using the same commercial software [29], the Coupled algorithm was employed to handle the pressure-velocity coupling. It was proved that this algorithm ensured more stable results when adopting different meshes, timesteps, or rotating speeds. The second order upwind scheme was used for spatial discretization of the whole set of RANS and turbulence equations, as well as the bounded second order for time differencing, to obtain good resolution.

Air was modeled as an ideal compressible gas with standard ambient conditions, i.e. a pressure of 1.01×10^5 Pa and a temperature of 300 K. The authors have recently presented an assessment of the main settings that have been applied to the CFD simulations [29], which have also been validated against experimental data obtaining very good agreement. The results of the sensitivity analyses on the main simulation parameters are here reported.

Exploiting the sliding-mesh model of the solver, the simulation domain was divided into two subdomains in order to allow the rotation of the turbine, as proposed by Maître et al. [30] and Raciti Castelli et al. [31]. Fig. 4 shows a circular zone containing the turbine, with a diameter (2D) twice that the turbine itself (D). R represents the turbine radius. The circular zone rotates with the angular velocity of the rotor while a rectangular fixed outer zone determines the overall domain extent.

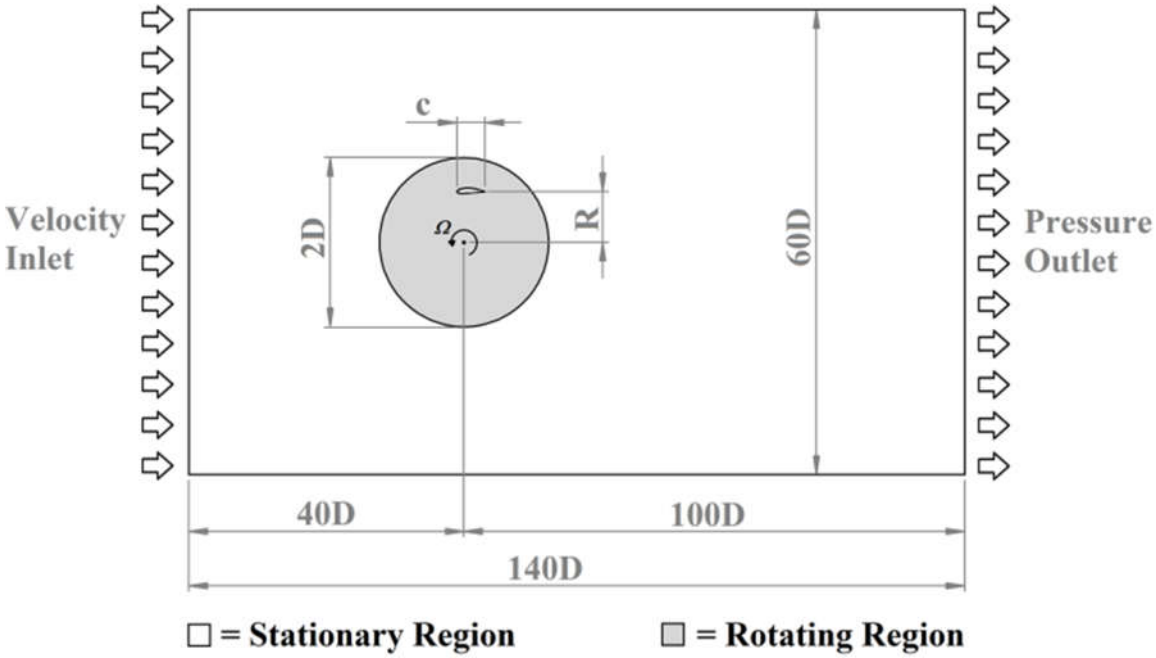

Figure 4 – Simulation domain.

The use of a sliding interface is of particular interest for unsteady simulations of rotating machines, thanks to the possibility of differentiating the discretization requirements between the two subdomains. The rotating region around the turbine has strict requirements in terms of spatial discretization, in order to correctly describe the flow gradients in the proximity of the blades. The outer region, conversely, often does not need extremely fine discretizations, allowing one to enlarge its overall dimensions to avoid undesired disturbances induced by the boundary conditions.

Focusing on this latter aspect, all the boundary distances of Fig. 4, selected after the sensitivity studies reported in [29], are given as a function of the rotor diameter. The velocity is imposed at the inlet section, which is placed 40 rotor diameters upwind of the rotating axis. The ambient pressure condition is imposed at the outlet boundary, located 100 rotor diameters downwind, while a symmetrical condition is defined for the lateral boundaries at a distance of 30 rotor diameters. The symmetry condition for lateral boundaries is the most common solution for this type of simulation (e.g. [32]). An alternative option could be to represent the lateral boundaries with “opening-type” conditions (i.e. able to support simultaneous inflow and outflow over a single region), which could

enable a reduction of domain width. Due to possible instabilities generated by this type of setting the conservative choice of symmetry conditions was maintained here.

Table 1 reports the main geometrical features of the four simulated models. The airfoil chord was kept constant in all the simulations, while the revolution radius was changed to achieve the two desired chord-to-radius ratios.

Table 1 – Test cases.

	Case 1	Case 2	Case 3	Case 4
c/R	0.114		0.25	
airfoil	NACA0018	Transformed (*c/R*=0.114)	NACA0018	Transformed (*c/R*=0.25)
c [m]	0.2	0.2	0.2	0.2
R [m]	1.75	1.75	0.8	0.8
U [m/s]	8	8	8	8

To correctly describe the flow around each airfoil, six different levels of refinement of the mesh and three angular time-steps were considered for both *c/R* ratios, in order to identify the required number of nodes in the mesh surrounding the airfoil and the total number of mesh elements of the computational grid. The mesh settings were defined accordingly to the results of the grid-independency analysis reported in [29], since they were deemed to guarantee the same level of accuracy.

An unstructured mesh composed by triangular elements was used for the discretization of the core flow region, except for the boundary layer region, where a structured O-grid was generated with a row of 50 inflated layers to include the entire boundary layer height. The requirement in terms of near wall refinement is very strict: the near-wall cell size is determined by imposing the condition that its first nodal point has a distance from the wall that does not exceed the limit required by a ω-based turbulence model for a proper resolution of the boundary layer. This was achieved by ensuring that the values of the dimensionless wall distance (y^+) during the rotor

revolution did not exceed the limit of 1, necessary to ensure that the first computational node falls in the linear region of the boundary layer.

The expansion ratio for the growth of elements starting from the surface was kept below 1.1 to achieve good mesh quality in proximity of the airfoil. It was proven that a grid-independent behavior can be obtained by using a discretization of the airfoil surface with approximately 600 nodes. The mesh size of the rotating region, for the single-bladed configuration, results in approximately 1.4×10^5 elements, while the stationary region is discretized with 2.0×10^5 elements. Figs 5-7 show some details of the grids. The rotating domain, containing the rotating blade, is characterized by a progressive coarsening of the elements with the distance from the blade. The mesh is refined in the region surrounding the blade due to the higher complexity of the flow field. As suggested by [31], a *control circle* (Fig. 6), with a diameter equal to twice the airfoil's chord, was defined around the blade in order to have a better capability to control the elements size in the region closer to the blade itself. The use of quadrilateral elements in the near-wall region is clearly distinguishable in Fig. 7 for the blade leading edge. The chosen mesh topology requires a grid-clustering in order to have a smaller spacing between the nodes near both the leading and trailing edges, being the regions experiencing the highest gradients.

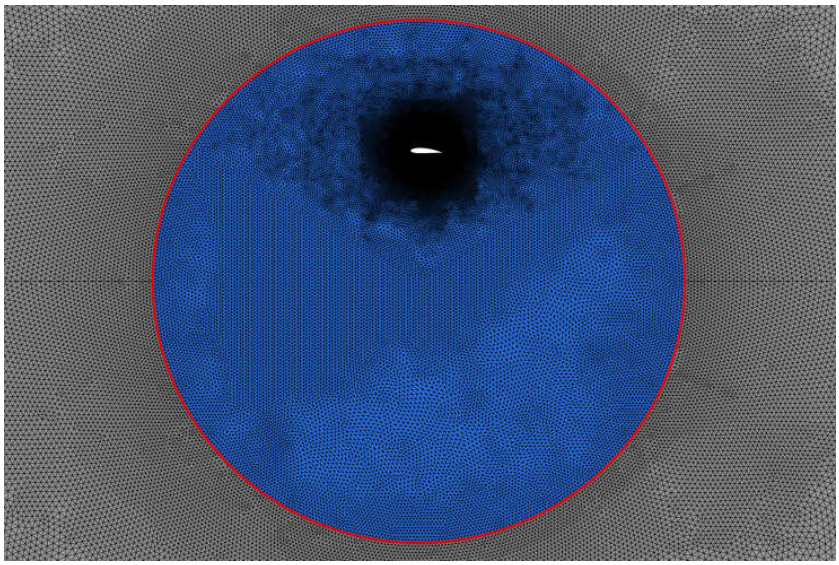

Figure 5 – Computational grid for the rotating domain (e.g. transformed airfoil with *c/R*=0.25).

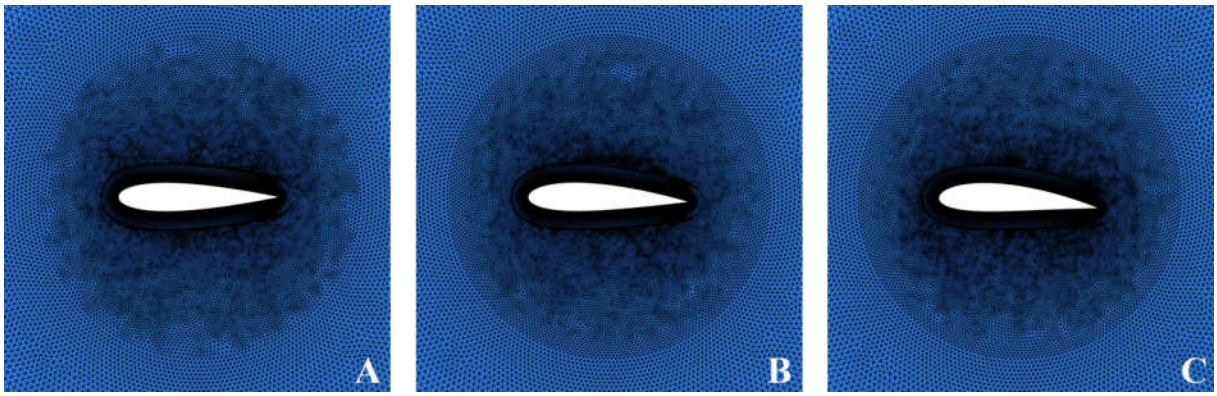

Figure 6 – Control circle details fort the NACA0018 (A), the transformed airfoil with *c/R*=0.114 (B) and *c/R*=0.25 (C).

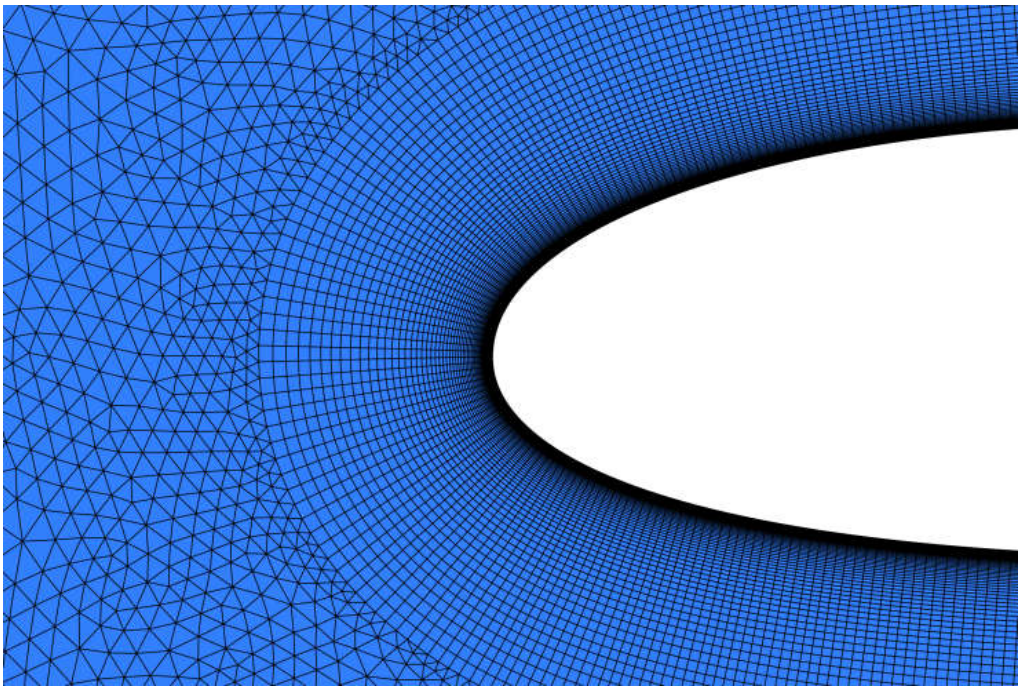

Figure 7 – Computational grid: boundary layer discretization at the leading edge (e.g. transformed airfoil with *c/R*=0.25).

Recent work [13] demonstrated that different functioning TSRs require specific minimum time steps in order to ensure accurate results. In the present analysis angular time steps in the

range between 0.135° and 0.42° were used, corresponding to the cases with the lowest and the highest TSR respectively.

As suggested by many authors (e.g. Howell et al. [33] or Rossetti et al. [34]), the global convergence of each simulation was monitored comparing the average value of the torque coefficient (c_T) over a complete revolution. After a specific sensitivity analysis [29], the selected threshold for convergence was identified in a variation lower than the 0.1% of the torque coefficient value between two subsequent revolutions. This value was by far lower than the limit commonly adopted in literature, i.e. 1%. The required number of revolutions is not a priori known, being dependent on the rotating speed of the turbine: in the present analyses, it ranged between 30 and 50 revolutions.

Concerning the turbulence closure problem, Balduzzi et al. [35], showed the effectiveness of Menter's shear stress transport (SST) model in performance simulations involving unsteady aerodynamics for VAWTs, as also confirmed by wide use in literature.

In the present study attention has been focused on a more detailed examination of the aerodynamic behavior of a single airfoil in motion by analyzing equivalent static pressure coefficients on the blade profiles. Since the prediction of the boundary layer evolution becomes a critical issue and the blade Reynolds number for the considered cases cannot guarantee a fully turbulent condition, the γ-Re_θ transition model (derived by Menter and Langtry from the SST model [36]) was implemented, despite its increased computational cost. Lanzafame et al. recently showed good agreement between experimental data and numerical results obtained with the transition turbulence model for two different types of H-Darrieus turbines [37].

The CFD methodology used in this study has been assessed and validated in the recent past through direct comparisons with experimental data. Simulations have been shown to accurately predict the experimental power curves of a full-scale rotor tested with variations of the pitch angle [13]. The methods also succeeded in correctly predicting blade torque profiles [29], as measured experimentally by Vittecoq and Laneville [38].

3.2 Data analysis

Once each simulation had reached full convergence, an additional revolution was simulated acquiring the pressure distribution over the airfoils and the flow field in proximity of the blades approximately every 2 degrees.

In order to reconstruct VAWT blade polars and evaluate the virtual camber effect, a robust procedure to extrapolate the incidence angle was needed. The concern of defining the angle of attack from CFD simulations of rotating blades has been addressed by wind turbine specialists in case of HAWTs [39]. More recently, a method for VAWTs was proposed by Balduzzi et al. [13] and then further improved by Bianchini et al. [20].

The method of Balduzzi et al. adapted the averaging technique of Hansen [40] for use in Darrieus turbines. In this method, the velocity triangles of the blades are reconstructed by evaluating the relative wind speed in a properly positioned area in front of the airfoil and applying an inverse BEM method to estimate the induction factor. In an inverse BEM method applied to VAWTs the effect of velocity reduction and distortion generated by the blade-flow interaction is globally modeled by a variation of the induction factor [13], with no information on the distortion of the absolute wind speed.

To overcome this intrinsic uncertainty, the novel approach developed by Bianchini et al. [20] was adopted, making use of the virtual camber concept, the main topic of the present study. The method, a four-step process, is briefly summarized here:

1. Based on the chord-to-radius ratio of the rotor (c/R) and the tip-speed ratio (TSR), the virtual airfoil due to flow-curvature effects is defined based on the conformal transformations of Migliore et al. [17].
2. The pressure coefficient distributions over the virtual airfoil are calculated for a wide range of AoAs with fine intervals of 0.25° between each. This is performed in XFoil [41] using a Reynolds number compatible with that attended on the airfoil. Then, all the pressure coefficient distributions are normalized within -1 and +1 by scaling them by their maximum

and minimum values. This solution allows comparison between pressure distributions, depending only on the incidence angle, with a negligible error on the exact relative speed, which can be hard to define from CFD calculations [20].

3. The pressure coefficient distributions calculated from CFD are acquired from calculations at different azimuthal positions and compared to those previously obtained for an airfoil with horizontal chord [13]. They are again normalized within -1 and +1 by scaling them by their maximum and minimum values.
4. For every azimuthal position, the pressure coefficient distribution from CFD is compared to all those calculated for the airfoils. By doing so, the distribution that best fits that from CFD can be highlighted. In particular, the position along the chord of the pressure peak is mainly used to define the incidence as the influence of flow speed has been discarded by normalizing the distributions. This comparison directly provides the estimation of the incidence on the airfoil. Moreover, by normalizing the pressure profile the relative speed can be evaluated *a posteriori*. This velocity value appeared fully compatible with that predicted based on the "reference zone estimation" of Ref. [13].

As discussed in literature [39], the validity of this approach unfortunately ceases as soon as the flow is separated around the turbine blades. In these conditions, no reliable blade pressure distribution can be obtained with XFoil and therefore no comparison can be made from CFD to XFoil to define the flow incidence on the airfoil.

4. Results

4.1 Wind tunnel experiments

Lift and drag coefficients for the three airfoils, tested at a Reynolds number of 300,000, are presented in Figs 8 and 9 respectively. The plots show coefficients for both increasing and decreasing incidence in the vicinity of stall. Results for the earlier NACA 0018 study of Timmer

[42], taken at the same Reynolds number, are also included. There is excellent agreement between the two NACA 0018 datasets, other than at stall points. Stall occurs at an incidence of 16° in the current study, with flow reattaching at 11° with decreasing incidence, with equivalent values in Timmer's study of 17° and 11.5° respectively. There are two possible causes for this difference:

Blockage effects – Timmer's data was taken in a conventional solid-walled tunnel and post-processed with blockage corrections. Though these corrections do adjust lift and drag to account for the acceleration of flow around the model caused by blockage, they do not account for the delay of stall to higher angles also caused by the faster flow. Since the tolerant tunnel used in this study physically reduces blockage, this problem is not encountered.

Airfoil surface finish – Both studies allowed free transition, were Timmer's models rougher than our own, higher stall/reattachment angles would be expected. Those of the current study were finished with 1000-grit sandpaper and paints (an accurate surface roughness measurement has not been obtainable). Timmer does not disclose surface roughness in his paper [42].

The "bump" in the lift coefficients of the two studies at around 8° is caused by a laminar separation bubble which Timmer was able to remove with application of zig-zag strips to initiate turbulent boundary layer transition.

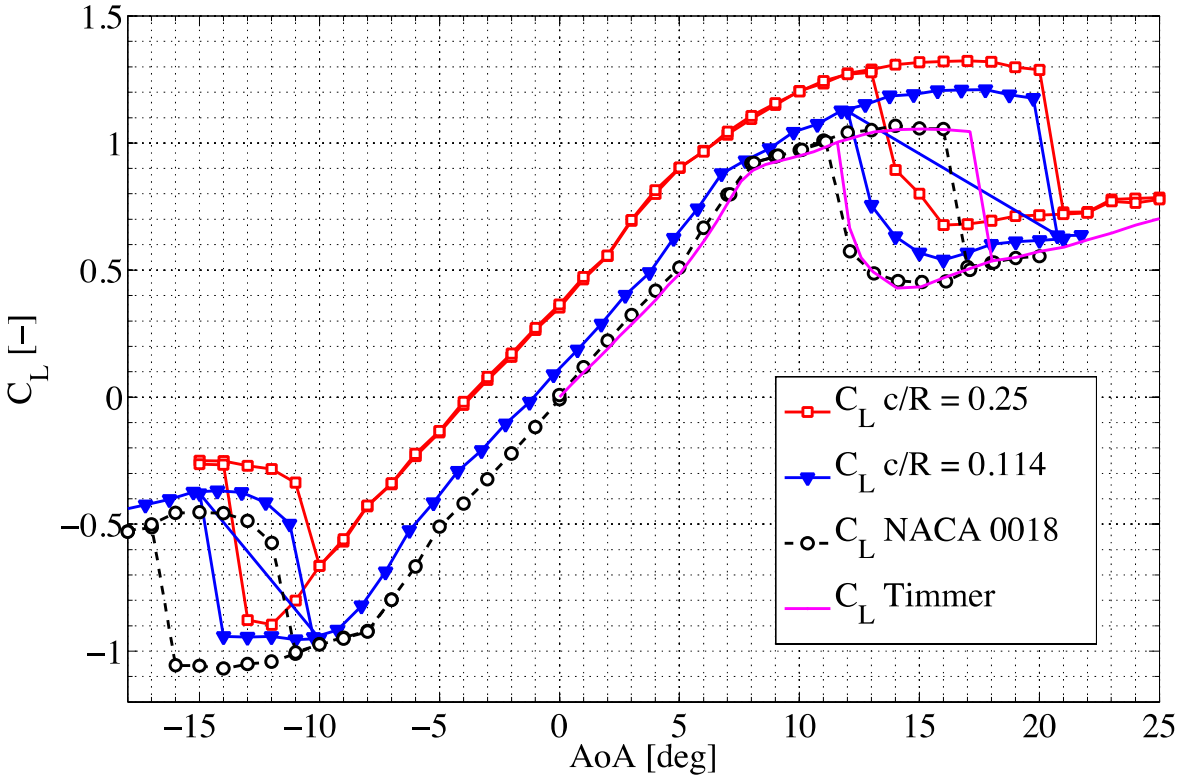

415

416 **Figure 8 – Lift against incidence for the NACA0018, Re = 300,000 (this study and Timmer [42]),**

417 **and for the *c/R* = 0.114 and *c/R* = 0.25 airfoils, Re = 300,000 (this study only).**

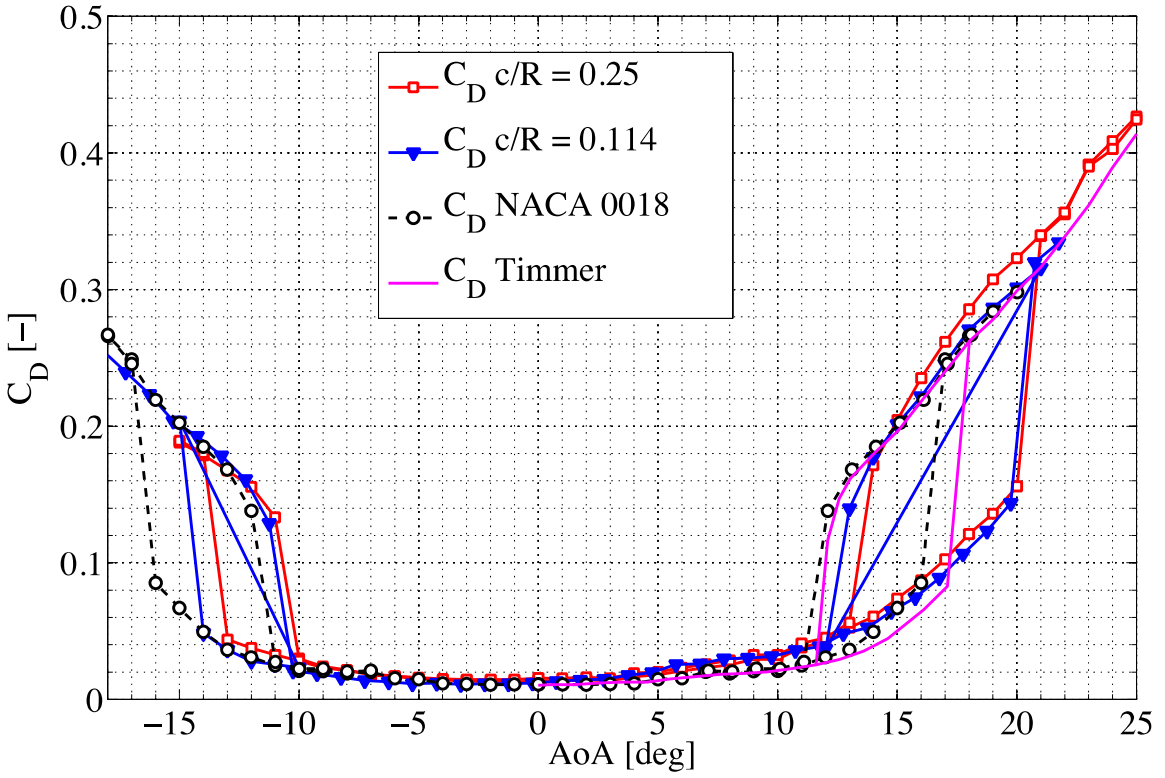

418

419 **Figure 9 - Drag against incidence for the NACA0018, Re = 300,000 (this study and Timmer [42]),**

420 **and for the c/R = 0.114 and c/R = 0.25 airfoils, Re = 300,000 (this study only).**

Since the two cambered airfoils were designed specifically for this study, there are no results in literature to compare them against. Figs 8 and 9 show them alongside results for the NACA 0018. The relationships between the aerodynamic characteristics and camber are as one would expect in this range of Reynolds numbers and blade thickness and cambers: the greater the camber, the higher the stall angle and Cl max at positive incidences, while the opposite is true at lower incidences, and the angle at which zero lift occurs decreases as camber increases [43].

4.2 CFD turbine simulations

For both chord-to-radius ratios, seven rotating speeds were considered for the simulation of the airfoils (the NACA0018 and the relevant transformed equivalent). An undisturbed wind speed of 8 m/s was imposed at the inlet boundary, leading to an investigated operating range of TSRs from 1.0 to 4.7. The comparison of power coefficients (c_P) trends is reported in Fig. 10 as a function of the tip speed ratio (TSR).

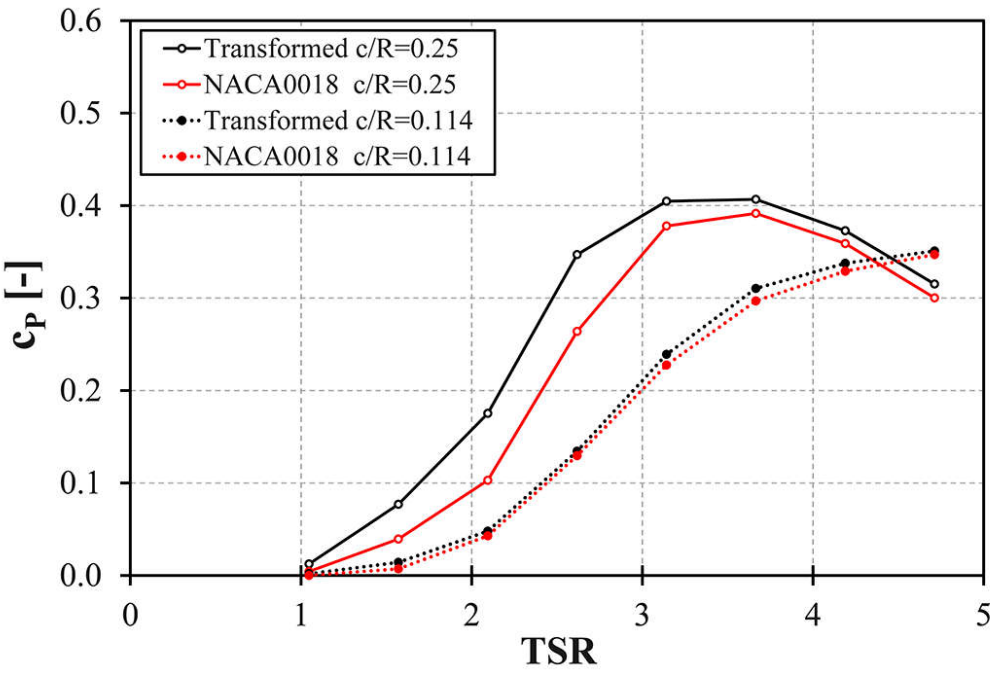

Figure 10 – Comparison of power coefficient curves for all the simulated airfoils.

As discussed in Bianchini et al. [20] and confirmed here, blades having a higher chord-to-radius ratio exhibit a shift of the curve peak towards lower TSRs. The behavior of the two airfoils at c/R = 0.114 are quite similar, while the two airfoils at c/R = 0.25 behave quite differently, stressing the importance of a proper blade design criteria for high c/R ratios [13]. These differences are also visible in torque extraction over the revolution, recently discussed by Bianchini et al. [20], who showed that the energy extraction with the transformed airfoil (arranged with its camber curving towards the center of rotation, and expected to behave like the symmetric NACA0018 in curvilinear flow) is more balanced between the upwind and the downwind halves of the revolution. Conversely, the geometrical NACA0018 (which in turn is expected to behave like the transformed airfoil with camber curved outward away from the center of rotation) concentrates the torque extraction in the upwind zone, providing higher local torque coefficients. Fig. 11 shows the tangential force coefficient over a revolution at TSR=3.1 for all the investigated airfoils, demonstrating this difference in upwind/downwind balance between the airfoils for c/R = 0.25.

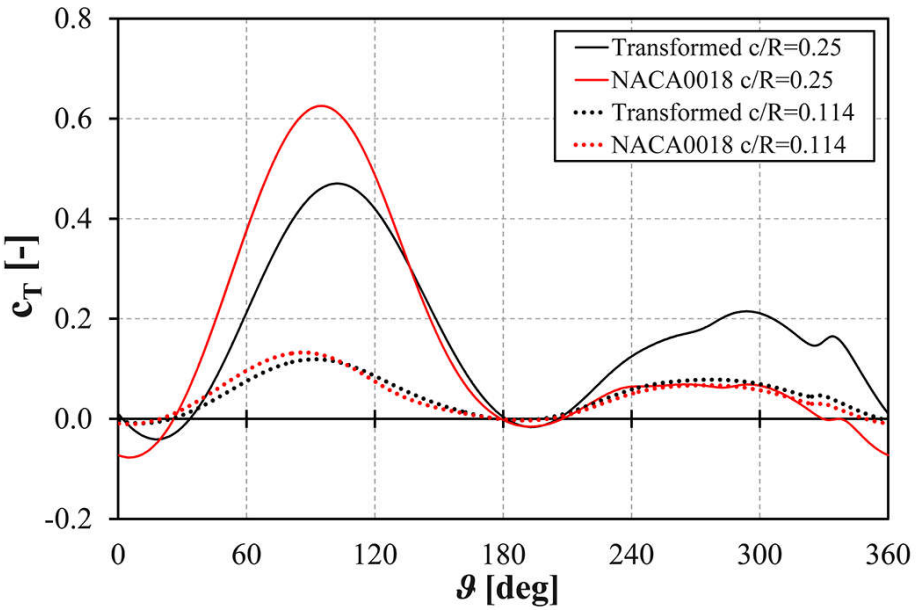

Figure 11 – Comparison of tangential force coefficient profiles over a revolution @ TSR=3.1 for all the simulated airfoils.

5. Discussion

To assess the impact of virtual camber effects on the aerodynamics of the airfoils in motion, two TSRs were selected for each curve and analyzed in detail. For both the c/R = 0.25 and the c/R = 0.114 cases, TSRs of 2.1 and 3.1 were selected. They are characterized by local blade Reynolds numbers between 2.5×10^5 and 3.0×10^5, comparable to those of the new experimental data collected in the wind tunnel.

For all the above operating conditions, the analysis was restricted to a range of azimuthal angles between approximately ϑ=-10° to ϑ=+70°. In this range, the AoA is generally small enough to ensure attached flow on the airfoil, allowing the procedure for AoA estimation by means of comparisons with XFoil data to be used. For the convention of signs and reference systems please refer to Fig. 12.

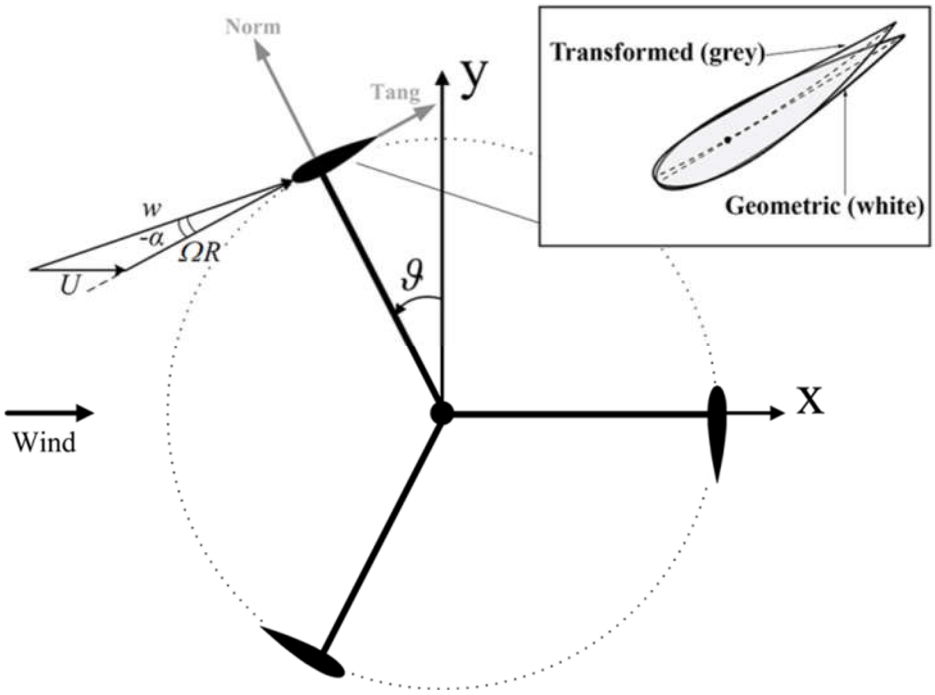

Figure 12 – Signs and reference systems convention.

The aforementioned procedure was applied to the selected azimuthal positions for all the tested airfoils. Based on previous results shown by Balduzzi et al. [13] and Bianchini et al. [18], the pressure coefficient distributions over the airfoils in every condition were expected to reproduce those of the corresponding virtual airfoil obtained from experiments on the conformal transformed airfoils. As mentioned, the transformed airfoil arranged with its camber inward becomes a virtual NACA 0018 when rotated about a radius four times its chord length, while the NACA 0018 becomes a virtual transformed airfoil with its camber outward in similar conditions (see Fig. 12).

The matching between the pressure profiles from CFD with those related to the virtual airfoil based on conformal transformation was excellent. As an example (comparable agreement was found in almost all the other considered azimuthal positions), Fig. 13 compares the pressure coefficient profiles at an azimuthal position of ϑ=32.8° of the four simulated airfoils with the correspondent distribution obtained with XFoil for the their equivalent transformed airfoils. With both the *c/R* ratios the virtual camber effect is verified. Also, the incidence angle (i.e. the angle of the pressure distribution over the virtual airfoils which best matched the CFD data) differs for the two configurations, as the two *c/R* ratios induce different virtual incidence effects, with a smaller incidence for the smaller c/R, again in line with virtual camber and incidence theory.

Finally, it is apparent that good agreement was also found between CFD and XFoil on the position of the transition on the airfoil.

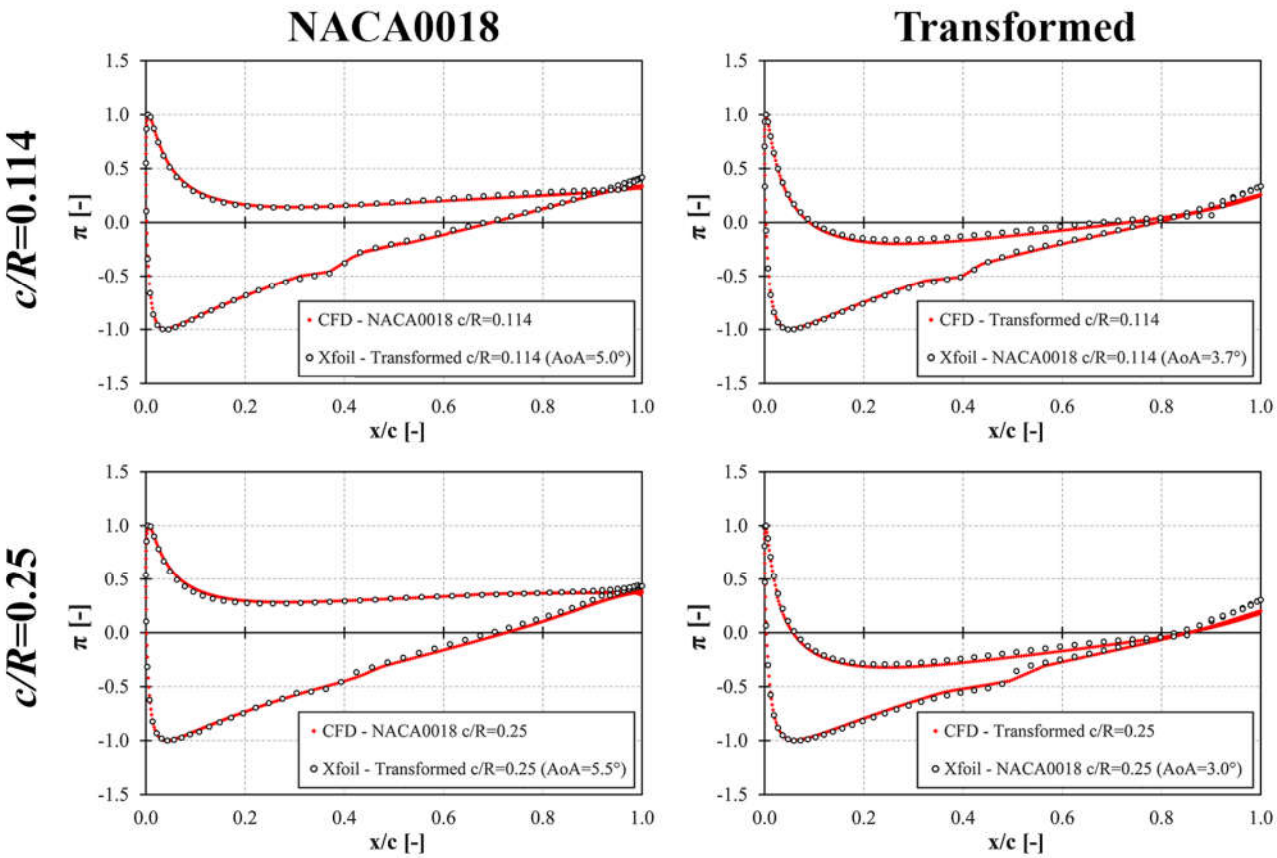

Figure 13 – Pressure profiles comparison @ ϑ=32.8°, TSR=3.1 for all the simulated airfoils: CFD data vs. matching profile over the transformed airfoil due to the virtual camber effect.

Once all the azimuthal positions were processed, the equivalent polars (i.e. the lift and drag outputs) of the airfoils during their revolution were reconstructed from the numerical evaluation of the tangential and normal forces exerted by the airfoils themselves.

Figs 14 and 15 show the trends for lift and drag coefficients, respectively, for all four airfoils in motion.

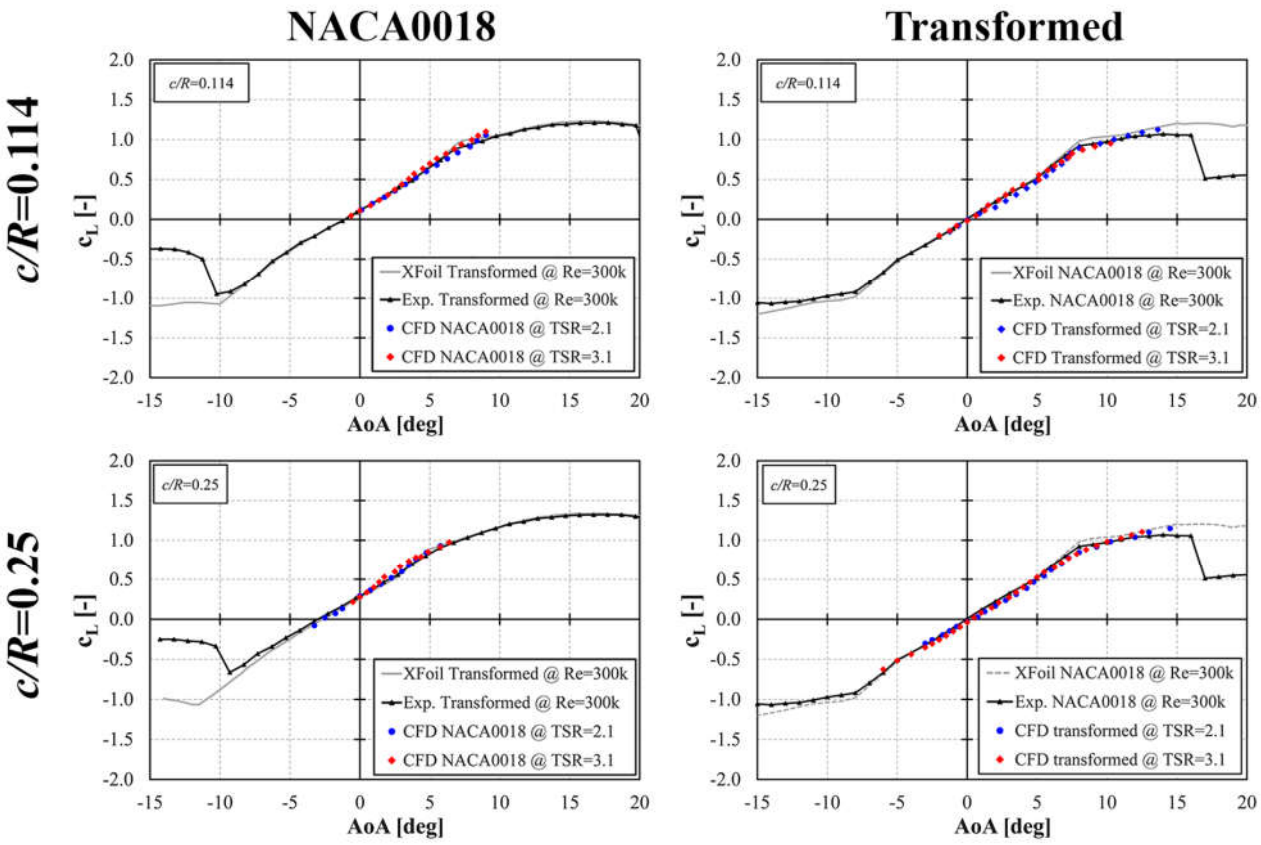

500

501 **Figure 14 – Reconstructed lift polars for the four simulated airfoils at TSR=2.1 and TSR=3.1.**

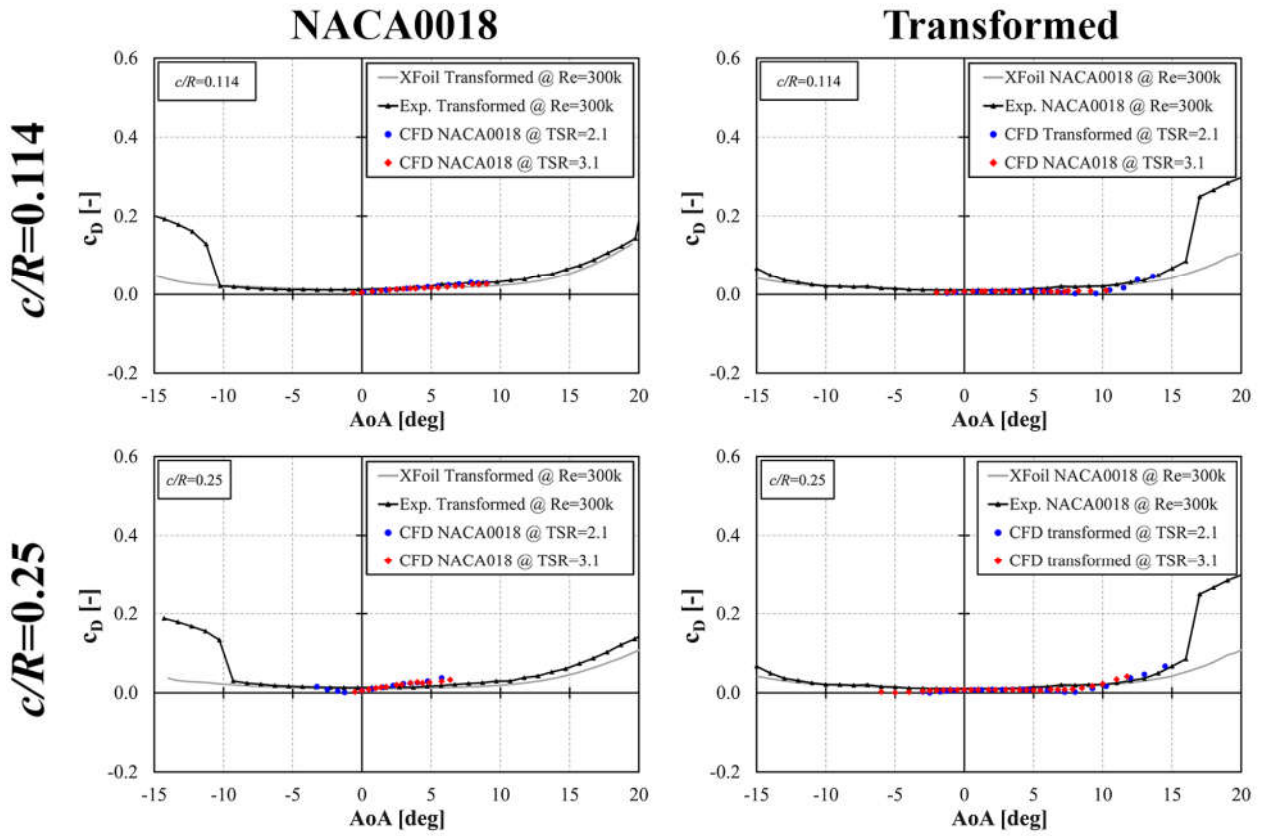

502

503 **Figure 15 – Reconstructed drag polars for the four simulated airfoils at TSR=2.1 and TSR=3.1.**

There is excellent agreement between reconstructed data from CFD and blade polars based on the equivalent virtual airfoil, whether calculated using XFoil or obtained experimentally. The lift coefficients are particularly well reproduced for both *c/R* ratios, in terms of both the slope of the linear region and the lift coefficient at AoA = 0°. Small discrepancies can be noticed in the drag coefficient produced by the CFD computed NACA0018 airfoil at the higher *c/R* ratio, which seems to increase more rapidly than that of the virtual transformed airfoil, although the very low absolute value of the drag is more sensitive to small errors produced by the analysis (e.g. in the correct estimation of the relative speed). Also, experiments used force transducers rather than a wake traverse to measure drag, which can be inaccurate where drag forces are very low.

It should be noted that since the incidence calculation technique works by matching CFD airfoil pressure distributions to the nearest match produced in XFoil, the incidences produced are inclusive of any virtual incidence effects. Thus, as mentioned, in Fig. 13 different incidences are calculated at different c/R ratios for the same airfoil, in spite of TSR and azimuth being the same, and the effects of virtual incidence have no impact on Figs 14 and 15.

All the above results clearly demonstrate that the virtual camber effect originally postulated Migliore et al [17] strongly affects the aerodynamic behavior of a Darrieus turbine with a medium-high chord-to-radius ratio. They also confirm the blade design criteria proposed by Balduzzi et al. [13] and demonstrate the suitability of the presented experimental data to the simulation of this type of wind turbine.

6. Potential benefits on BEM analyses

The main use of the results obtained in the present work is connected to their potential impact on BEM models. Though more advanced prediction models are available (e.g. CFD or vortex models), these simplified theories can still provide some advantages under defined

529 circumstances, especially concerning the general design of a machine (e.g. overall dimensions
530 and attended power) and particularly when a reduction of the computational cost is needed [18].
531 Based on a lumped parameters approach to aerodynamics, BEM models are intrinsically very
532 sensitive to the accuracy of input blade data in terms of lift and drag coefficients [44].
533 Discrepancies in tabulated data, even small, can substantially affect the reliability of the
534 predictions, both in terms of peak efficiency and of optimal TSR.
535 To quantify the effect of neglecting virtual camber, experimental coefficients collected in the
536 wind tunnel (and matched by CFD) were used in the VARDAR BEM code of the University of
537 Florence, which has previously been validated against experimental results for a Darrieus turbine
538 taken in a wind tunnel [18] and is considered a robust design tool for H-Darrieus rotors [45].
539 Using the code, two turbine geometries were simulated either with the lift and drag
540 coefficients of the NACA 0018 or with those of the equivalent transformed airfoil at each *c/R*
541 ratio. Figs 16 and 17 report the comparison in terms of power coefficient curves between CFD
542 and BEM with turbine *c/R* = 0.114 and *c/R* = 0.25 respectively.
543

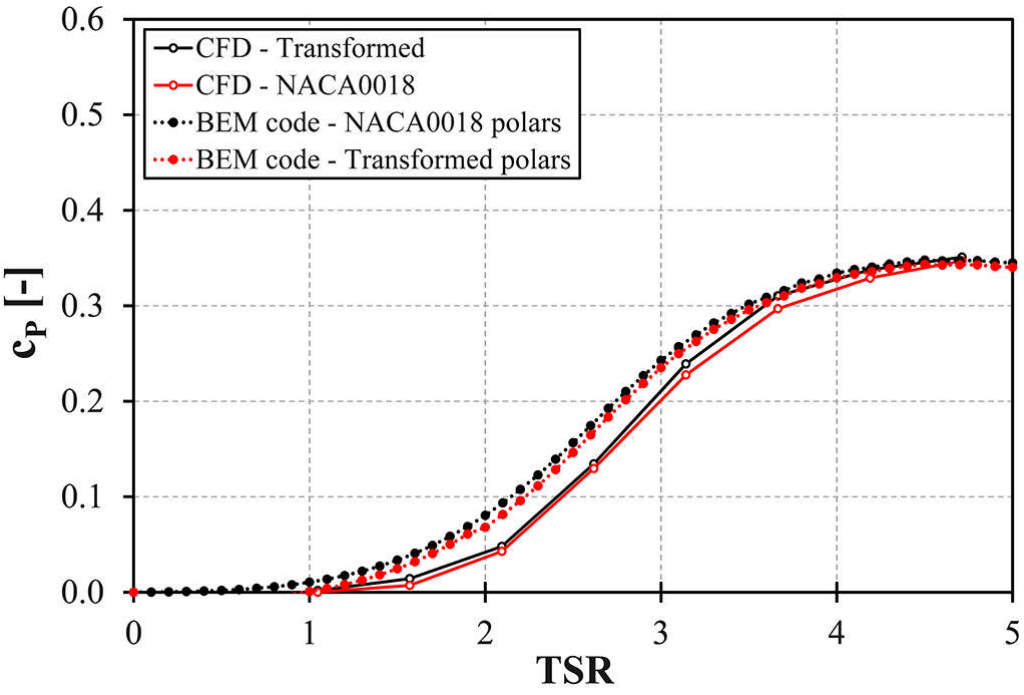

544

545 **Figure 16 – Comparison between BEM and CFD based power coefficient curves at *c/R*=0.114.**

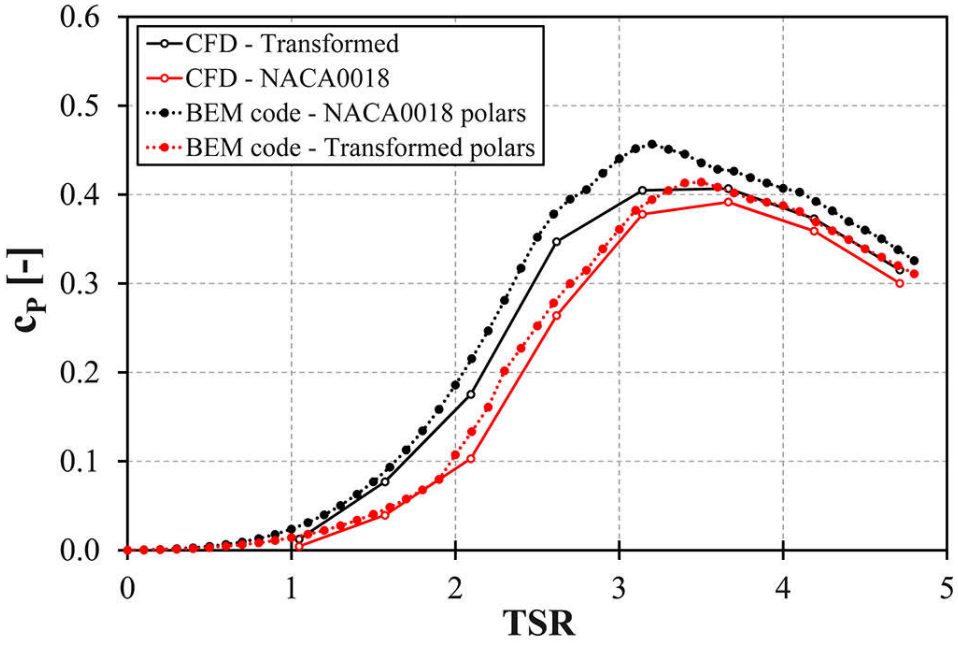

Figure 17 – Comparison between BEM and CFD based power coefficient curves at *c/R*=0.25.

For the c/R = 0.25 case, BEM predictions using the polar of the virtually transformed airfoil fit the 2D CFD simulation of the NACA 0018 well, and similarly BEM results for the NACA 0018 fit the CFD simulation of the transforms. Agreement between BEM and CFD simulations using the same blade profiles is clearly worse. Agreement for the *c/R* = 0.114 case is strong between the two CFD simulations and the two BEM simulations, suggesting the impact of virtual camber is less extreme on the outputs of the two codes at this lower *c/R*.

The impact of virtual camber on the reliability of the code for the *c/R* = 0.25 case is more pronounced if the predictions of blade torque production as a function of the azimuthal position of the blade is analyzed. Fig. 18 compares the torque profile of the CFD transformed airfoil at TSR = 3.1 with the predictions of the BEM code using the coefficients of the transformed airfoil and the NACA 0018. The agreement is far stronger between the transformed airfoil and the virtually equivalent NACA 0018 than with its geometrical equivalent.

The use of the aerodynamic coefficients of the equivalent transformed airfoil appears necessary for an accurate prediction of behavior using a BEM model when the *c/R* ratio is high, with a remarkable improvement in the agreement of this theory to CFD.

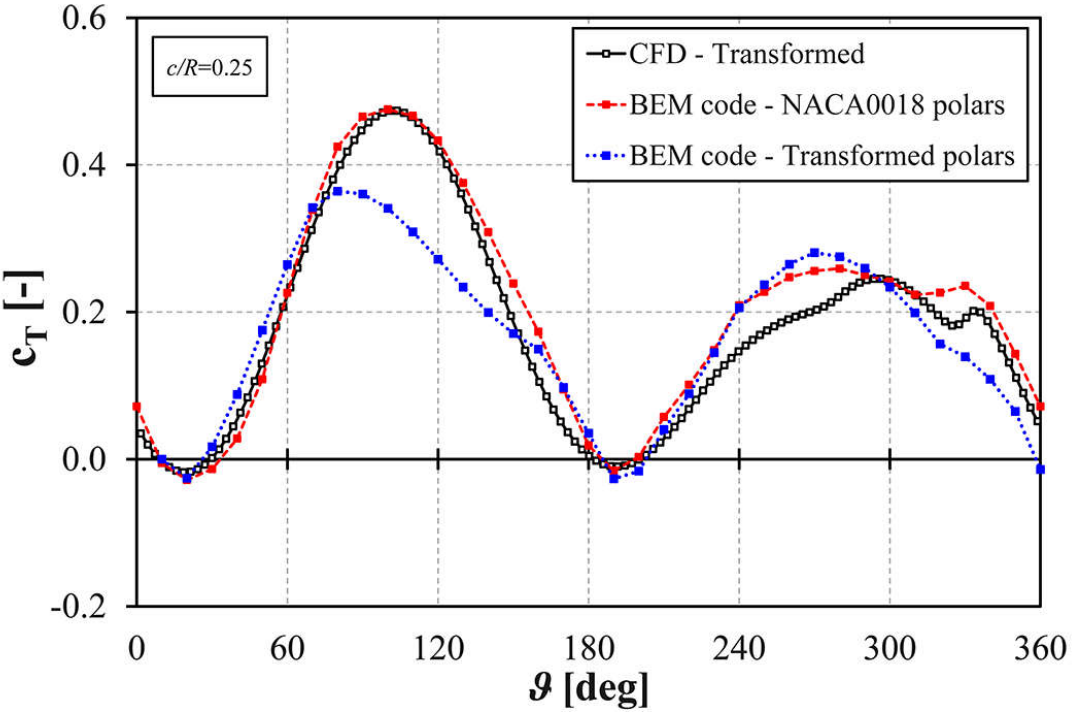

Figure 18 – Tangential force coefficient trends @ TSR=3.14 and *c/R*=0.25: CFD simulation of the transformed airfoil vs. BEM predictions using different polars.

7. Conclusions

Results have been presented in a study analyzing the impact of virtual camber effects on the performance of Darrieus VAWT blades. The curved paths blades follow have been hypothesized to impart virtual camber and incidence on them, making their behavior analogous to cambered airfoils in rectilinear flow. Comparisons have been made between results from wind tunnel tests in rectilinear flow on a NACA 0018 and two blades modified to exhibit the virtual camber expected in VAWTs with *c/R* = 0.114 and 0.25, and CFD simulations of the curvilinear flow of VAWT blades for the same three profiles.

Curves of lift and drag against incidence computed from the CFD results match not to the same profile from the wind tunnel work, but to the relevant equivalent virtually transformed profile. This suggests that virtual camber is a significant contributor to VAWT performance and as such must be considered when making use of low order models such as BEM codes.

An analysis is made of VAWT performance in terms of power coefficient against TSR using BEM with the experimental polars of the three airfoils, alongside a similar analysis using CFD. For higher *c/R* ratios, there is again good agreement between relevant transformed pairings and not between geometrically identical airfoils. This agreement extends to a blade-level analysis prepared using the BEM and the CFD in the form of blade tangential force coefficients against azimuth.

Findings show that consideration of curvature effects is necessary to obtain accurate results from BEM codes that are comparable to those of CFD. When simulating a VAWT using BEM methods, blade data for input should be selected based not on the physical geometry of the blade, but on that of a transformed profile. The profile should have camber such that its chord aligns with an arc of the circumference of the turbine. Such profiles can be calculated using conformal transformation theory. The incidence of this transformed blade should be adjusted in line with Migliore's virtual incidence. If experimental data is not available for the transformed profile, it can be obtained using the methods described in this paper, or estimated (for attached flows) by simulating the transformed airfoil shape using panel methods.

8. Acknowledgments

We would like to thank Prof. Ennio Antonio Carnevale of the University of Florence for supporting this research program. Experimental work was supported financially by the Environmental Services Association Education Trust.

9. Nomenclature

Acronyms

AoA	Angle of Attack
BEM	Blade Element Momentum
CFD	Computational Fluid Dynamics
OAR	Open Area Ratio
SST	Shear Stress Transport
TSR	Tip-Speed Ratio
U-RANS	Unsteady Reynolds-Averaged Navier-Stokes
VAWTs	Vertical Axis Wind Turbines

Greek symbols

α	Angle of Attack (symbol)	[deg]
γ	Intermittency	
ϑ	Azimuthal Angle	[deg]
π	Dimensionless Pressure Coefficient	[-]
ω	Specific Turbulence Dissipation Rate	[1/s]
Ω	Revolution Speed	[m/s]

Latin symbols

A	Turbine's Swept Area	[m^2]
c	Blade Chord	[m]
c_D	Drag Coefficient	[-]
c_L	Lift Coefficient	[-]
c_P	Power Coefficient	[-]

624	c_T	Tangential Force Coefficient	[-]
625	D	Rotor Diameter	[m]
626	Ft	Tangential Force	[N]
627	g	Slatted Wall Spacing	[m]
628	k	Turbulence Kinetic Energy	[m^2/s^2]
629	L	Plenum Chamber Length of the Tolerant Tunnel	[m]
630	p	Plenum Chamber Depth of the Tolerant Tunnel	[m]
631	R	Rotor Radius	[m]
632	Re	Reynolds Number	[-]
633	Re_θ	Momentum Thickness Reynolds Number	[-]
634	s	Slatted Wall Distance	[m]
635	U	Undisturbed Wind Speed	[m/s]
636	w	Relative Speed	[m/s]
637	y^+	Dimensionless Wall Distance	[-]

638

10. References

[1] Global Wind Energy Outlook. GWEC, Brussels (Belgium); 2014.

[2] Small Wind Turbine Global Market Study. AWEA, Whashington DC (USA); 2008.

[3] Dayan E. Wind energy in buildings: Power generation from wind in the urban environment - where it is needed most. Refocus 2006;72(2):33-38.

[4] Balduzzi F, Bianchini A, Ferrari L. Microeolic turbines in the built environment: influence of the installation site on the potential energy yield. Renewable Energy 2012;45:163-174. DOI**:** 10.1016/j.renene.2012.02.022

[5] Mertens S. Wind Energy in the Built Environment. Brentwood (UK): Multi-Science; 2006.

[6] Kirke BK, Evaluation of self-starting vertical axis wind turbines for standalone applications. Ph.D. thesis, Griffith University, Gold Coast (Australia); 1998.

[7] Balduzzi F, Bianchini A, Carnevale EA, Ferrari L, Magnani S. Feasibility analysis of a Darrieus vertical-axis wind turbine installation in the rooftop of a building. Applied Energy 2012;97:921–929. DOI: 10.1016/j.apenergy.2011.12.008

[8] Simão Ferreira CJ, van Bussel G, van Kuik G. An analytical method to predict the variation in performance of a H-Darrieus in skewed flow and its experimental validation. Proc. of the European Wind Energy Conference, February 27-March 2, 2006, Athens (Greece); 2006.

[9] Bianchini A, Ferrara G, Ferrari L, Magnani S, An improved model for the performance estimation of an H-Darrieus wind turbine in skewed flow. Wind Engineering 2012;36(6):667-686. DOI: 10.1260/0309-524X.36.6.667

[10] Bianchini A, Ferrara G, Ferrari L, Design guidelines for H-Darrieus wind turbines: Optimization of the annual energy yield. Energy Conversion and Management 2015;89:690-707. DOI: 10.1016/j.enconman.2014.10.038

[11] Aslam Bhutta MM, Hayat N, Farooq AU, Ali Z, Jamil ShR, Hussain Z, Vertical axis wind turbine – A review of various configurations and design techniques. Renewable and Sustainable Energy Reviews 2012;16(4):1926-1939. DOI: 10.1016/j.rser.2011.12.004

[12] Paraschivoiu I, Wind Turbine Design with Emphasis on Darrieus Concept. Polytechnic International Press, Canada; 2002.

[13] Balduzzi F, Bianchini A, Maleci R, Ferrara G, Ferrari L. Blade design criteria to compensate the flow curvature effects in H-Darrieus wind turbines. Journal of Turbomachinery 2015;137(1):1-10. DOI: 10.1115/1.4028245

[14] Borg M, Shires A, Collu M, Offshore floating vertical axis wind turbines, dynamics modelling state of the art. Part I: Aerodynamics. Renewable and Sustainable Energy Reviews 2014;39:1214-1225. DOI:10.1016/j.rser.2014.07.096

[15] Bianchini A, Ferrari L, Magnani S. Start-up behavior of a three-bladed H-Darrieus VAWT: experimental and numerical analysis. Proc. of the ASME Turbo Expo 2011, Vancouver (Canada), June 6-10; 2011. DOI: 10.1115/GT2011-45882

[16] Camporeale SM, Magi V. Streamtube model for analysis of vertical axis variable pitch turbine for marine currents energy conversion. Energy conversion and Management 2000;41(16):1811-1827. DOI: 10.1016/S0196-8904(99)00183-1

[17] Migliore PG, Wolfe WP, Fanucci JB, Flow curvature effects on Darrieus turbine blade aerodynamics. Journal of Energy 1980;4(2):49-55. DOI: 10.2514/3.62459

[18] Bianchini A, Ferrari L, Carnevale EA, A model to account for the virtual camber effect in the performance prediction of an H-Darrieus VAWT using the momentum models. Wind Engineering 2011; 35(4):465-482. DOI: 10.1260/0309-524X.35.4.465

[19] Rainbird J, Peiro J, Graham JM, Post-stall airfoil performance and vertical-axis wind turbines. 33rd ASME wind energy symposium, AIAA SciTech 2015, Kissimmee, Florida, USA, Jan 5-9, 2015.

[20] Bianchini A, Balduzzi F, Rainbird J, Peiro J, Graham JMR, Ferrara G, Ferrari L, An Experimental and Numerical Assessment of Airfoil Polars for Use in Darrieus Wind Turbines. Part 1 - Flow Curvature Effects. Journal of Engineering for Gas Turbines and Power 2016;138(3). DOI: 10.1115/1.4031269.
[21] http://www.ugei.com/vertical-axis-wind-turbine/visionair3-vawt, last access 09/2015.
[22] M. S. Selig, C. A. Lyon, P. Giguere, C. Ninham, and J. Guglielmo, *Summary of low-speed airfoil data vols. 1-5*, SoarTech Publications, Virginia Beach, VA, 1995-2012.
[23] Althaus, D., *Profilpolaren für den Modellflug, vols. 1 & 2*. Neckar-Verlag, Villingen-Schwenningen. 1980.
[24] ESDU, Lift-interference and blockage corrections for two-dimensional subsonic flow in ventilated and closed wind-tunnels. Technical Report 76028, Engineering Sciences Data Unit, 1978.
[25] Khoo H, Separated flow past wind turbine aerofoil sections. Thesis (M.Phil.) - Department of Aeronautics, Imperial College, London 1991.
[26] Hill N, Dominy R, Ingram G, Dominy J, Darrieus turbines: the physics of self-starting. Proceedings of the Institution of Mechanical Engineers Part A-Journal of Power and Energy 2009;223:21-29.
[27] Parkinson G, The tolerant tunnel: concept and performance. Canadian Aeronautics and Space Journal 1990;36(3):130-134.
[28] Ansys, Inc., 2013, Fluent Theory Guide, release 14.5. 4.
[29] Balduzzi F, Bianchini A, Maleci R, Ferrara G, Ferrari L, Critical issues in the CFD simulation of Darrieus wind turbines. Renewable Energy 2016;85(01):419-435. DOI: 10.1016/j.renene.2015.06.048
[30] Maître T, Amet E, Pellone, C. Modeling of the Flow in a Darrieus Water Turbine: Wall Grid Refinement Analysis and Comparison with Experiments. Renewable Energy 2013;51:497–512. DOI: 10.1016/j.renene.2012.09.030
[31] Raciti Castelli M, Englaro A, Benini E. The Darrieus Wind Turbine: Proposal for a New Performance Prediction Model Based on CFD. Energy 2011;36(8):4919–4934. DOI: 10.1016/j.energy.2011.05.036
[32] Beri H, Yao Y. Effect of Camber Airfoil on Self Starting of Vertical Axis Wind Turbine," *J.* Environ. Sci. Technol. 2011;4(3):302–312.
[33] Howell R, Qin N, Edwards J, Durrani N. Wind Tunnel and Numerical Study of a Small Vertical Axis Wind Turbine. Renewable Energy 2010;35(2):412–422. DOI: 10.1016/j.renene.2009.07.025
[34] Rossetti A, Pavesi G. Comparison of Different Numerical Approaches to the Study of the H-Darrieus Turbines Start-Up. Renewable Energy 2013;**50**(February):7–19. DOI: 10.1016/j.renene.2012.06.025
[35] Balduzzi F, Bianchini A, Gigante FA, Ferrara G, Campobasso MS, Ferrari L, Parametric and Comparative Assessment of Navier-Stokes CFD Methodologies for Darrieus Wind Turbine Performance Analysis, Proc. of the ASME Turbo Expo 2015, Montreal, Canada, June 15-19, 2015. DOI: 10.1115/GT2015-42663
[36] Menter FR, Langtry RB, Likki SR, Suzen YB, Huang, PG., and Völker, S., A Correlation-based Transition Model Using Local Variables Part 1 – Model Formulation, Proc. of the ASME Turbo Expo 2004, Vienna, Austria, June 14-17, 2004.
[37] Lanzafame R, Mauro S, Messina M, 2D CFD modeling of H-Darrieus wind turbines using a transition turbulence model. Energy Procedia 2014;45:131-140.
[38] Vittecoq P, Laneville A, The aerodynamic forces for a Darrieus rotor with straight blades: Wind tunnel measurements. Journal of Wind Engineering and Industrial Aerodynamics 1983;15(1-3):381-388.

[39] Guntur, S. and Sørensen, N.N., 2012, "Evaluation of several methods of determining the angle of attack on wind turbine blades," Proc. of The science of Making Torque from Wind 2012, Oldenburg, Germany, 09-11 October 2012.
[40] Hansen, M.O.L., Sørensen, N.N., Sørensen, J.N., and Michelsen J.A., 1997, "Extraction of lift, drag and angle of attack from computed 3-D viscous flow around a rotating blade," Proc. of the EWEC 1997, Dublin (Ireland), pp. 499–501.
[41] XFoil User Guide, available online at: http://web.mit.edu/drela/Public/web/xfoil, last access 02/10/2014
[42] Timmer WA, Two-dimensional low-Reynolds number wind tunnel results for airfoil NACA0018. Wind Engineering 2008;32(6):525-537.
[43] Jacobs EN, Sherman A, Airfoil section characteristics as affected by variations of the Reynolds number. Tech. Rep. 586, NACA, 1937.
[44] Bianchini, A., Balduzzi, F., Rainbird, J., Peiro, J., Graham, J M.R., Ferrara, G. and Ferrari, L., 2015, "An Experimental and Numerical Assessment of Airfoil Polars for Use in Darrieus Wind Turbines. Part 2 - Post-Stall Data Extrapolation Methods," Journal of Engineering for Gas Turbines and Power 2016;138(3). DOI: 10.1115/1.4031270
[45] Bianchini A, Ferrari L, Magnani S., Energy-yield-based optimization of an H-Darrieus wind turbine. Proceedings of the ASME Turbo Expo 2012, Copenhagen (Denmark), June 11-15, 2012. DOI: 10.1115/GT2012-69892